Satellite-derived river width and its spatiotemporal patterns in China during 1990–2015

Jie Yang[a], Xin Huang[a,b,*], Qiuhong Tang[c,d,*]

[a] School of Remote Sensing and Information Engineering, Wuhan University, Wuhan 430079, PR China
[b] State Key Laboratory of Information Engineering in Surveying, Mapping and Remote Sensing, Wuhan University, Wuhan 430079, PR China
[c] Key Laboratory of Water Cycle and Related Land Surface Processes, Institute of Geographic Sciences and Natural Resources Research, Chinese Academy of Sciences, Beijing 100101, PR China
[d] College of Resources and Environment, University of Chinese Academy of Sciences, Beijing 100049, PR China

ABSTRACT

Rivers are essential to the Earth's ecosystem, but the current understanding of river width variability is limited, owing to the sparse distribution of gauging stations. Remote sensing data enable the surveying and analysis of river geomorphology by providing multi-temporal Earth observation data from satellites at fine spatial and temporal resolutions. We proposed an optimized RivWidth method to automatically calculate width for all channels in a water map and parallelized it to produce the Multi-temporal China River Width (MCRW) dataset, which is the first 30-m multi-temporal river width dataset for China during 1990–2015, including estimates under both seasonal fluctuations and dynamic inundation frequencies. The MCRW dataset is made up of 1.3×10^8 seasonal estimates of river width, and covers 1.4×10^5 km of rivers in China. We validated the MCRW dataset against in-situ measurements. The MCRW estimates at maximum water extent showed a satisfactory accuracy of 15.0% and 15.2% for the mean absolute percentage error (MAPE) and the relative root-mean-square error (RRMSE), respectively. The MCRW dataset was further compared with the current state-of-the-art global product, the Global River Widths from Landsat (GRWL) dataset, which demonstrated the superiority of the MCRW in describing the basins of China. Our analysis indicated that the mean river widths of China in both summer and winter have increased over the past 25 years, and river width of the Yangtze River mainstream in the lower drainage region has shown a downward trend while the its middle reaches and tributaries (upstream of the Three Gorges Dam) have shown an upward trend. We also developed a locally adaptive search method to quantify seasonal (summer and winter) river width variability. The results revealed that most of the rivers were wider in summer during the study period, and mainstream of Yangtze River in middle/lower region exhibited less seasonal variability than its tributaries. Larger widths were observed in the middle reaches of the Yellow River and the upper reaches of the Black River in winter due to ice-jam floods. Overall, the generated MCRW dataset has the potential to serve as a fundamental resource in Earth system science, and could provide valuable support to surface water resource and riverine management.

1. Introduction

Fluvial networks are the dominant mechanism by which surface water is delivered from land to ocean, providing a host of vital ecosystem services, e.g., water purification, nutrient cycles, flood relief, and hydropower (Tang et al., 2009). Simultaneously, rivers are crucial emitters of greenhouse gas, and are responsible for a substantial amount of carbon dioxide and methane outgassing to the atmosphere (Bastviken et al., 2011; Battin et al., 2008; Raymond et al., 2013). Consequently, knowledge of the location and persistence of river geomorphology, such as river width, is crucial for water resource assessments (Gleason and Smith, 2014; Mueller et al., 2016; Yamazaki et al., 2012; Sichangi et al., 2016; Van Dijk et al., 2016; Tarpanelli et al., 2019; Yang et al., 2019; Van Dijk and Renzullo, 2011; Tang, 2020), water-related hazard prevention (Zong and Chen, 2000), and river morphodynamics (Monegaglia et al., 2018). In the context of river monitoring, in-situ gauge observations are the foundation of the current understanding of river width dynamics (Alsdorf et al., 2003). Given this context, a thorough understanding of river width fluctuations could provide practical support for decision-makers to implement effective

and sustainable management. However, a stream gauge network can only provide point-based observations of riverine environments (Alsdorf et al., 2007). Furthermore, in-situ observations of river width are often lacking, due to the sparse distribution of gauges.

With the global gauge network shrinking due to the high maintenance costs (The Ad Hoc Group et al., 2001; Hrachowitz et al., 2013; Hannah et al., 2011), alternative methods for estimating river width in ungauged basins have been developed in recent years. Such methods usually incorporate river widths generated by field survey or manual measurement from aerial or satellite images (Barefoot et al., 2019; Biancamaria et al., 2009; Gurnell, 1997; Wilson et al., 2007; Xu et al., 2004). However, the manual interpretation is laborious and time-consuming, even for small basins. With respect to large rivers, their widths are usually estimated by the empirical relationships with streamflow (Andreadis et al., 2013; Sun et al., 2018; Yamazaki et al., 2012; Hou et al., 2020; Hou et al., 2018) or drainage area (de Paiva et al., 2013; Hou et al., 2019). Nevertheless, such empirical functions cannot capture the variations of river channels since hydrologic and geologic conditions can vary in different river segments and over time. Furthermore, it remains unclear whether a consistent empirical function of river width can serve as a fundamental parameter in regional- or global-scale models (Yamazaki et al., 2014).

It has been widely recognized that remote sensing enables an improved understanding of the Earth by gathering multi-temporal observations from orbiting platforms at a fine spatial resolution. Landsat satellites, for instance, have been collecting multispectral images of the Earth at a 30-m spatial resolution since 1984 with the launch of Landsat 5, forming an accessible global archive courtesy of the Landsat Global Archive Consolidation (LGAC) initiative (Wulder et al., 2016). Hence, continually updated remote sensing data, in conjunction with the recent advances in cloud-based platforms such as the Google Earth Engine (Gorelick et al., 2017), have the potential to provide us with a viable source of observations, plus the computational capabilities to generate large-scale datasets of river geomorphology, thus ensuring a better understanding of river width dynamics. In a pioneering effort, Yamazaki et al. (2014) developed the Global Width Database for Large Rivers (GWD-LR) using Shuttle Radar Topography Mission (SRTM) Water Body Data (SWBD) and the HydroSHEDS (Hydrologic data and maps based on Shuttle Elevation Derivatives at multiple Scales) (Lehner et al., 2008) flow direction map. However, by using SWBD data as baseline data, GWD-LR has limited coverage for river channels narrower than 300 m. To address this limitation, recent efforts have been focused toward large-scale fine-resolution river width products, such as the North American River Width (NARWidth) (Allen and Pavelsky, 2015) and GRWL (Allen and Pavelsky, 2018) datasets. The NARWidth dataset was constructed by calculating the width of North American rivers at mean discharge by applying an automated width determination tool—RivWidth (Pavelsky and Smith, 2008)—to the Landsat-derived water map. In addition, Isikdogan et al. (2017) developed river width data for North American rivers by estimating river center lines and widths directly from a 3-year Landsat composite, showing a comparable accuracy with NARWidth.

While automated river geomorphology and width determination algorithms can be found in the existing literature (Table 1), in all these studies, however, the river geomorphology has been presented under certain climate or hydrologic conditions. For instance, GWD-LR only provides the river width during the period when SRTM data were acquired, and NARWidth was composited by sorted cloudless Landsat images captured at mean annual discharge. While the hydrologic and hydraulic models have long been multi-temporal, observational multi-temporal river width are generally unavailable. Due to the fine spatial and temporal coverage of satellite images, the satellite-derived multi-temporal river width datasets can offer more comprehensive characterizations of river width dynamics under different climate or hydrologic conditions over large extent (e.g., regional to global scale).In addition, as there are increasing hydrological or hydraulic modeling

Table 1

The existing satellite-derived river width datasets. Temporal coverage is not available for NARWidth and GWD-LR since they were generated using Landsat (TM, ETM +, and OLI) images acquired at mean discharge. Temporal coverage is also not available for Lin et al., (2020) as their dataset follows a time-invariant assumption. Bank to bank width represents the width measured perpendicular to the river center line at each pixel, while the wetted width excludes in-water islands.

Name and abbreviation	Spatial coverage	Baseline data	Temporal coverage	Width type	Nominal resolution	Data source
Global Width Database for Large Rivers (GWD-LR)	Global	SRTM	11/Feb/2000 to 22/Feb/2000	Bank to bank & Wetted	90 m	Yamazaki et al., 2014
North American River Width (NARWidth)	North American	Landsat	N/A	Wetted	30 m	Allen and Pavelsky, 2015
North American River Width from RivaMap	North American	Landsat	2013–2015 composite	Wetted	30 m	Isikdogan et al., 2017
Global River Widths from Landsat (GRWL)	Global	Landsat	N/A	Wetted	30 m	Allen and Pavelsky, 2018
Hydromorphological attributes for all Australian river	Australia	Landsat	1987–2014	Wetted	25 m	Hou et al., 2019
Global reach-level bankfull river width using machine learning	Global	Landsat	N/A	Bank to bank	30 m	Lin et al., 2020
Multi-temporal China River Width (MCRW)	China	Landsat	1990–2015 Summer & winter	Wetted	30 m	This study

studies using vectorized river network (Lin et al., 2019), the dynamic river width data can provide important reference for the modeling studies. Moreover, multi-temporal datasets of river width can provide insights into the impacts of anthropogenic activities and changes in fluvial geomorphology, and can subsequently help the authorities to act more efficiently (Isikdogan et al., 2017). In addition, it has long been recognized that river width varies throughout the year in response to precipitation changes (Burn, 1999; Zong and Chen, 2000). In China, seasonal precipitation fluctuations are dominated by the warm-humid East Asian summer monsoon and the cold-dry East Asian winter monsoon (An et al., 1990). However, to the best of our knowledge, the current understanding of river width dynamics in China remains incomplete.

To address the absence of multi-temporal datasets of river width and the lack of understanding of the spatiotemporal dynamics of river width in the drainage regions of China, the objectives of this study were: (i) to generate a multi-temporal river width dataset for China; and (ii) to analyze the spatiotemporal dynamics of river width in China from 1990 to 2015. To achieve these goals, we: i) generated the first multi-temporal river width dataset of China (i.e., Multi-temporal China River Width dataset, MCRW), including estimates under both seasonal fluctuations (summer and winter) and dynamic inundation frequencies; ii) proposed a locally adaptive search method to further analyze the spatial-temporal patterns and seasonal variations of river width of China; and iii) improved RivWidth method by preserving the channel structures as well as saving memory and computation time. The accuracy of the estimated river width was validated with respect to in-situ measurements and by comparison with the existing datasets. To the best of the authors' knowledge, the existing research has rarely investigated the spatiotemporal patterns of river width variations via satellite remote sensing data. Although there have been multi-temporal datasets developed at smaller scales, this is the first paper that investigates the spatiotemporal patterns of river width at the country level, with special attention paid to river width variations under both seasonal fluctuations and dynamic inundation frequencies. The outcome of this study—the Multi-temporal China River Width dataset (MCRW)—can provide continual dynamic width measurements along river channels. Such a dataset could be used in hydrologic studies, pollutant dispersion, and flood models.

2. Study area

The primary goal of this study was to generate a multi-temporal river width dataset of China (Fig. 1). Located in East Asia, China covers a land area of over 9.6 million square kilometers and embraces a multitude of exterior rivers (e.g. the Yangtze and Yellow Rivers) that stem from the Qinghai-Tibet Plateau, and interior rivers (e.g. the Tarim River), which drain more than one-third of its territory. Climatologically, China is an interesting research area as its annual precipitation mostly occurs in the rainy season when the moist East Asian summer monsoon usually begins in May and retreats in August, while the dry East Asian winter monsoon surges in December and weakens in February (Wang and Ho, 2002). Based on the climatological characteristics, we focused on two seasons for all the rivers of China: summer (May to September) and winter (November to March). Geographically, the study area was stratified into nine major drainage regions based on rivers and their connected tributaries: the Inland River region (ILR), the Songliao River region (SLR), the Yellow River region (YLR), the Hai River region (HAR), the Huai River region (HHR), the Pearl River region (PER), the South-West River region (SWR), the South-East River region (SER), and the Yangtze River region (YZR) (Fig. 1).

3. Methodology

This study was aimed at developing the MCRW dataset and revealing the spatiotemporal dynamics and seasonal variability of river

widths in China. Our method consisted of three steps. We first composited 12 seasonal river maps using the Global Surface Water (Pekel et al., 2016) dataset to indicate the persistence and location of the rivers in summer and winter for the six periods (i.e., 1990, 1995, 2000, 2005, 2010, and 2015). An improved RivWidth method was then proposed to automatically calculate width for all channels in a given map. We also developed a multi-processing framework to accelerate the parallel execution of the width estimation method across multiple river maps. Finally, we developed a locally adaptive search method to further analyze the spatial-temporal patterns and seasonal variations of river width of China.

3.1. Generation of the multi-temporal China River width dataset

3.1.1. Compositing seasonal water maps

The input images for large-scale optical remote sensing analysis should adequately minimize the non-valid observations from clouds, snow, or other disturbances. These images can be composited using massive amounts of data, according to specific criteria, e.g., cloud cover and temporal span (Grinand et al., 2013; Lück and van Niekerk, 2016). Unfortunately, accessing and managing vast volumes of remote sensing data for large-scale analysis is strenuous and resource-intensive. The Google Earth Engine (GEE) has overcome these obstacles through Google's massive computational and storage capabilities, together with a multi-petabyte archive consisting of publicly available images (e.g., Landsat, MODIS, Sentinel), climate datasets, socioeconomic data, and an advanced function library for parallel processing, which enables large-scale geospatial data analysis (Gorelick et al., 2017). GEE's dedicated data distribution models have empowered a paradigm shift from traditional per-scene analysis to per-pixel analysis, which enables us to make pixel-wise cloudless composites (Azzari and Lobell, 2017; Donchyts et al., 2016). Therefore, we utilized the GEE platform to composite cloud-free, seamless images via multi-temporal complementation.

The monthly history collection of the Global Surface Water (GSW) dataset was employed as the basis to obtain the aforementioned seasonal water maps in the six periods (i.e., 1990, 1995, 2000, 2005, 2010, and 2015). The GSW dataset was generated using 3 million Landsat scenes, with the omission error less than 5% and the commission error less than 1% (Pekel et al., 2016). The GSW monthly history collection provides information on whether surface water appeared at the monthly level from Mar/1984 to Oct/2015. We first combined the GSW monthly data as a 5-year composite for each study period, e.g., all the monthly data available from 2003 to 2007 were combined for the nominal year of 2005. To describe the seasonal fluctuations, the images of each period were then divided into two seasonal groups, i.e., winter: November–March, and summer: May–September (Fig. 2). We extended the winter season from November to March since the surface water data in GSW are not always available during the winter in scenes where the solar elevation is larger than a specific threshold (see Section 5.3 for details). Finally, each seasonal group was reduced into a single composite for each pixel, respectively, by computing the water occurrence under three conditions (i.e., 1%, 50%, 100%). This approach of using all the available seasonal images enabled us to: (i) maximize the likelihood that the composited water maps were acquired across the summer/winter monsoons; (ii) maximize the coverage of GSW in each time period; and (iii) minimize the contamination from clouds, snow, or other disturbance, while preserving the seasonal variations of river width. The 12 resulting composites (Fig. 2) had a 30-m resolution and each composite included a binary label (1 for water and 0 for non-water) to indicate the persistence and location of surface water in summer/winter.

Please notice that the width measurements in the cases of 1%, 50% and 100% water occurrence for each period represented the maximum (1% occurrence), mean (50% occurrence) and minimum (100% occurrence) river width, respectively (Hou et al., 2019). The water
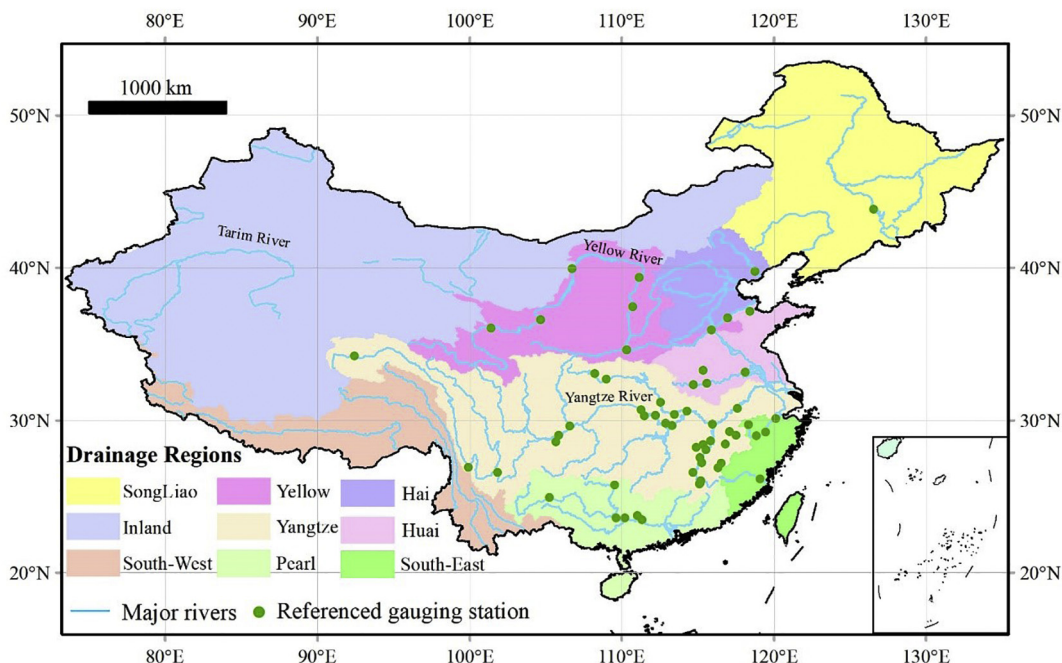
Fig. 1. The nine drainage regions of China and the gauging stations used for the validation. The nine river basins are the Inland River Region (ILR), the Songliao River Region (SLR), the Yellow River Region (YLR), the Hai River Region (HAR), the Huai River region (HHR), the Pearl River region (PER), the South-West River region (SWR), the South-East River region (SER), and the Yangtze River region (YZR). (For interpretation of the references to colour in this figure legend, the reader is referred to the web version of this article.)

occurrence was defined as:

$$\frac{WD}{VO} \tag{1}$$

where *WD* denoted the total water detections during a period (e.g., summer or winter for a certain year) and *VO* stands for the total valid observations (e.g., free of cloud, snow, and missing data) during the same period. Please notice that the water occurrence in this study is different from the occurrence layer in the GSW. We calculate the water occurrence during a period (e.g., summer or winter for a certain year) while the GSW occurrence layer is based on the data over 30 years.

Several processes were further conducted using the GEE platform to delineate rivers from the binary water map (Fig. 3). In order to obtain the outer banks of rivers, gaps within the water maps whose area was less than 9 km², e.g., islands and sandbars, were filled in. Meanwhile, we filtered out the isolated water bodies (usually ponds and irrigated lands) whose area is less than a threshold of 2700 m² (~ 4 ha), in terms of their normal size in the study area. We excluded reservoirs and lakes using the Global Reservoir and Dam Database (Lehner et al., 2011) and the Global Lakes and Wetlands Database (Lehner and Döll, 2004), since this research was only focused on rivers.

3.1.2. Calculating the multi-temporal river width

An automatic algorithm is needed to estimate river width from the river maps. The existing methods (e.g. RivWidth, RivaMap) have demonstrated their effectiveness in generating large-scale river width datasets (Allen and Pavelsky, 2015, 2018; Isikdogan et al., 2017; Miller et al., 2014). Functionally, RivWidth requires a binary water map with water and non-water pixels as input, and uses trigonometry to calculate the width at each pixel in the river center line. To estimate river width from the binary river maps, RivWidth first measures the Euclidean distance for each water pixel to the nearest non-water pixel using
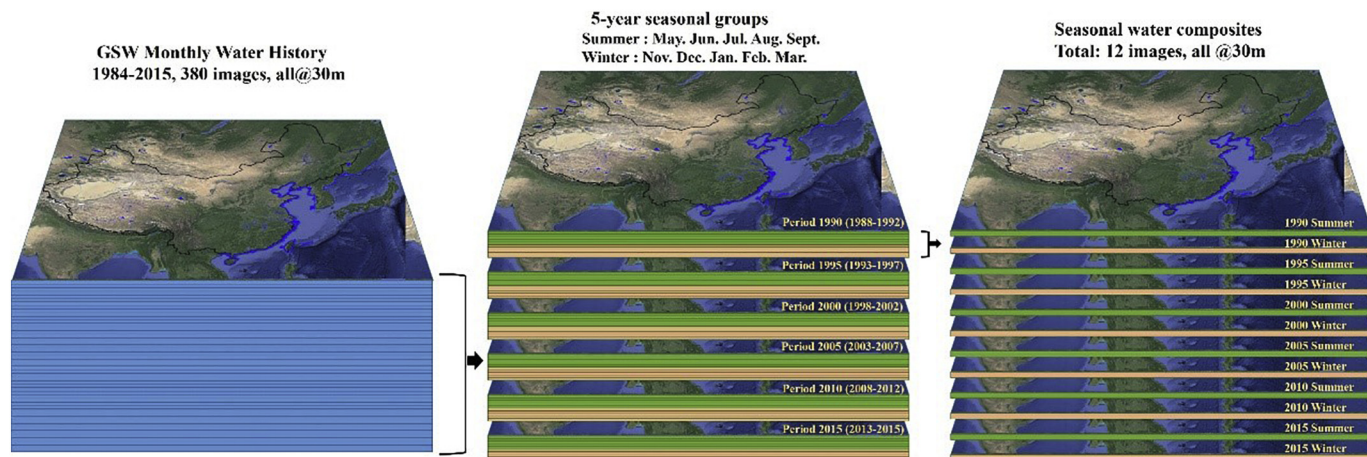

Fig. 2. 30-m seasonal water maps of China composited for six periods (i.e., 1990, 1995, 2000, 2005, 2010, 2015) using Global Surface Water (GSW) monthly water data. For each period, the GSW data for summer/winter were composited at a 5-year interval (e.g., period 1990: 1988–1992).
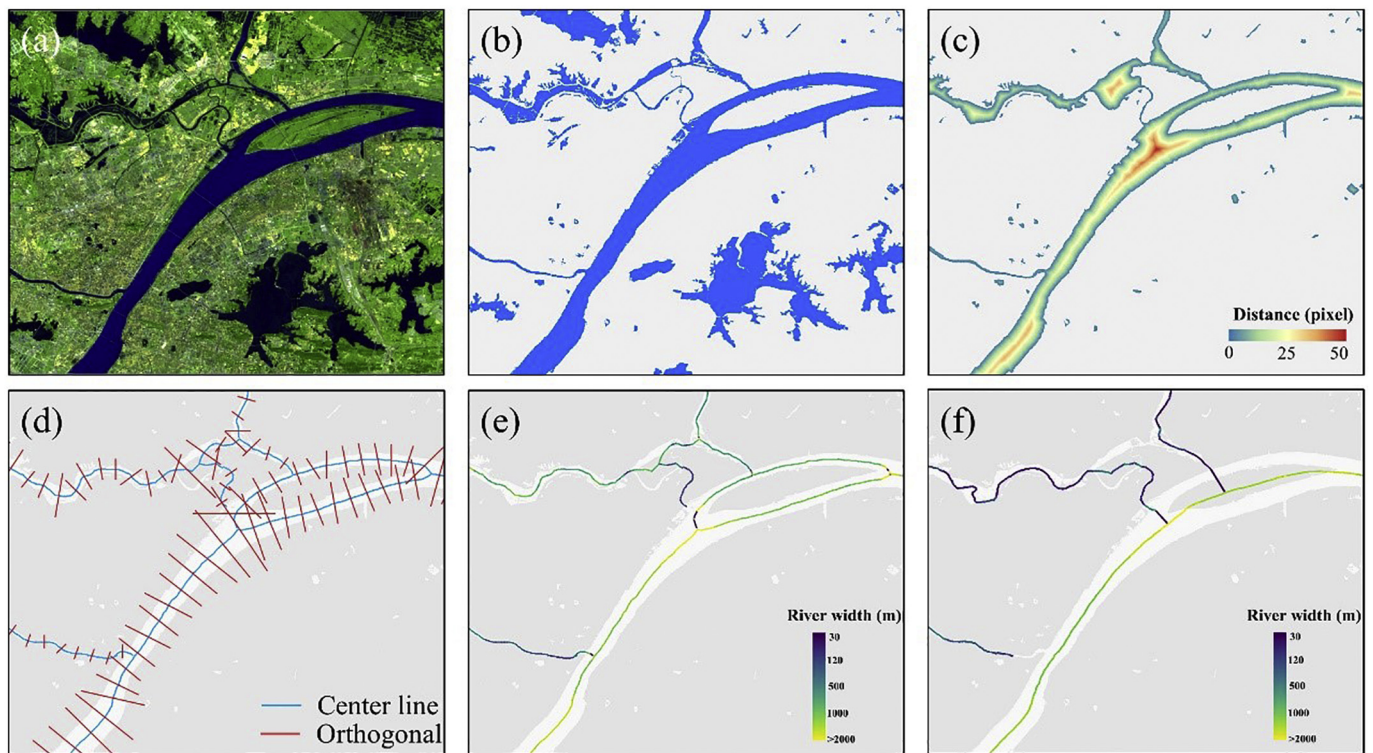
Fig. 3. Inputs, intermediate steps, and outputs of the calculation of river width in this study: (a) false colour percentile (20%) composite of Landsat 8 for middle reach of the Yangtze River (30.6363 N, 114.3425 E); (b) composited seasonal GSW water map; (c) distance map based on morphology distance transform; (d) river center line (blue) and orthogonal (red), orthogonals are presented every 30 pixels for visualization purposes only; (e) MCRW maximum measurements in 2015 summer; (f) GRWL width measurements at mean discharge(derived by RivWidth). (For interpretation of the references to colour in this figure legend, the reader is referred to the web version of this article.)

Table 2
Comparison of computation time, demonstrating the performance of our modification in reducing the computational time.

MCRW tile id	Major River	Time consumption (with modification)	Time consumption (without modification)
30N_90E	Yarlung Zangbo River	1874.9 s	53,459.9 s
27N_114E	Pearl River	1078.4 s	35,835.5 s

morphological distance transform (Rosenfeld and Pfaltz, 1968) (Fig. 3b). The distance map is then convolved with a bidirectional La-placian filter (Marr et al., 1980) to find the center line of each river channel (Fig. 3c). Finally, the river width is calculated by adding up the width of channels intersected by each orthogonal transect (Pavelsky and Smith, 2008). Thereby, the performance of RivWidth depends on the accuracy of the input water maps. RivaMap, on the other hand, estimates river center lines and widths directly from water-enhanced images (e.g. the Modified Normalized Difference Water Index, MNDWI) (Xu, 2006). The effects of RivaMap rely on the performance of the MNDWI and a series of post-processing algorithms to isolate snow and shadows from water (Isikdogan et al., 2017). The method of RivWidth was chosen in our research since: (i) it is able to automatically extract river widths from the input binary water map; (ii) many rivers in China originate from the mountains in the Qinghai-Tibet Plateau, where snow and shadows show high MNDWI responses, leading to a large number of errors when adopting the RivaMap method. In this study, therefore, we improved the RivWidth (version 0.4) method, and used the multi-sea-sonal river surface data derived from the GSW dataset as the input to calculate the river width for all the river channels of China longer than 1500 m.

In this research, the RivWidth algorithm was modified by a series of optimized strategies. Specifically, we first search for the largest river in a given river map and then calculated its width. Subsequently, we re-moved this river and applied RivWidth to the remaining largest one. In

such way, we were able to traverse all the channels in the water map and calculate their widths. Moreover, during each iteration, river width was estimated within a buffer area for each channel network, rather than the whole map, considering the fact that the channels only account for a small portion of the map. In this way, a lot of memory and com-putation time (e.g., convolution operations used to find connected components) can be saved while ensuring the effectiveness of the al-gorithm at the same time. Two typical examples, Yarlung Zangbo River and Pearl River, were shown in Table 2.

In addition, RivWidth removed all islands and sandy bars in the river channel and calculated the wetted width based on the center line of their outer banks. In such case, multi-channel rivers are aggregated into a single one. To preserve the river's original structure, we attempt to obtain the center line of each channel and measure its width in-dividually (Fig. 3e).

In particular, in the cases of multi-channel or braided rivers, where the flow directions changed rapidly, river width may be overestimated since cross sections derived from flow directions to each center line pixel were not completely orthogonal to the channel (Allen and Pavelsky, 2015; Miller et al., 2014). In this research, specifically, when a river is braided or has multiple channels (e.g., Fig. 4b), and the area of its surrounding islands or sandy bars was smaller than a threshold, its center line was delineated using outer banks of the entire river (Fig. 4e) and its width was calculated by summing up the wetted width of channels (Fig. 4d) intersected by each orthogonal. Please note that the
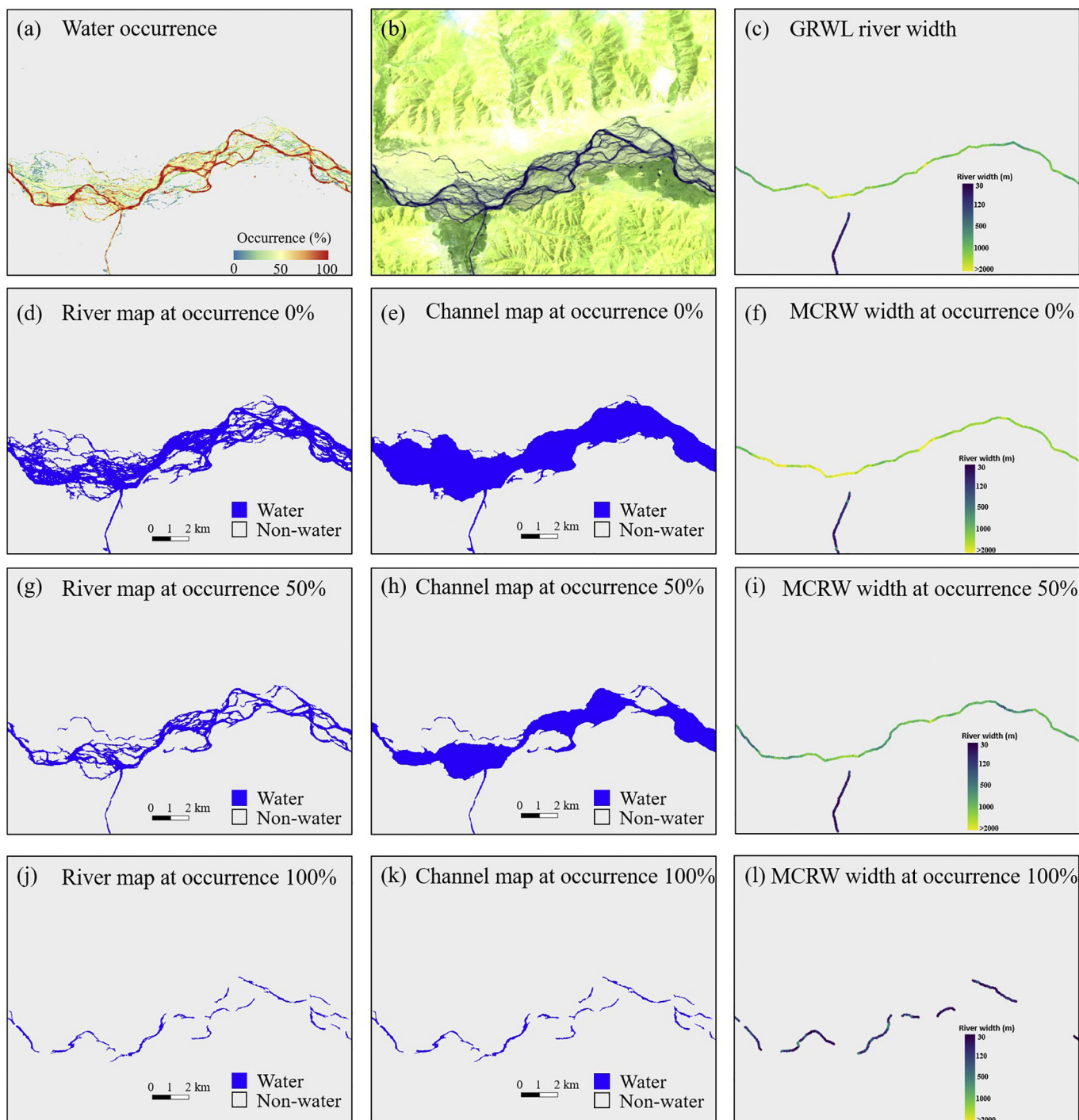
Fig. 4. Illustration of the data and results of width estimation for braided rivers: (a) GSW occurrence map showing the percentage of times surface water was observed in 2005 summer; (b) false colour median-value composite of Landsat-5 data for upper reach of Yarlung Zangbo River located on 29.37 N and 88.94 E; (c) GRWL river width at mean discharge; (d), (g) and (j) are composited river maps at 1%, 50% and 100% occurrence, respectively; (e), (h) and (k) are channel maps that only used to delineate the center line at 1%, 50% and 100% occurrence, respectively; (f), (i) and (l) are MCRW river widths at 1%, 50% and 100% occurrence, respectively.

number of channels that each orthogonal intersected at center line as well as the end points of each orthogonal were provided as supplementary information with each MCRW measurement.

To further estimate the river widths of China in multiple periods, we divided each seasonal river map into 81 tiles of 3° latitude by 6° longitude, and each tile was buffered by 0.2° to avoid boundary artifacts. In order to fully leverage the multi-core processors of computers, we designed a multi-processing framework in Interactive Data Language (IDL) to process all the tiles in parallel. This framework is mainly composed of a process pool that maintains a set of ready-to-use child processes (Fig. S1), and a supervising process that schedules image tiles for asynchronous execution over the child processes. The supervising process keeps tiles waiting in the queue when all the child processes are busy, and it allocates a waiting tile for the concurrent execution after the child process completes the river width estimation from the previous tile. This pool-based parallelism enables us to
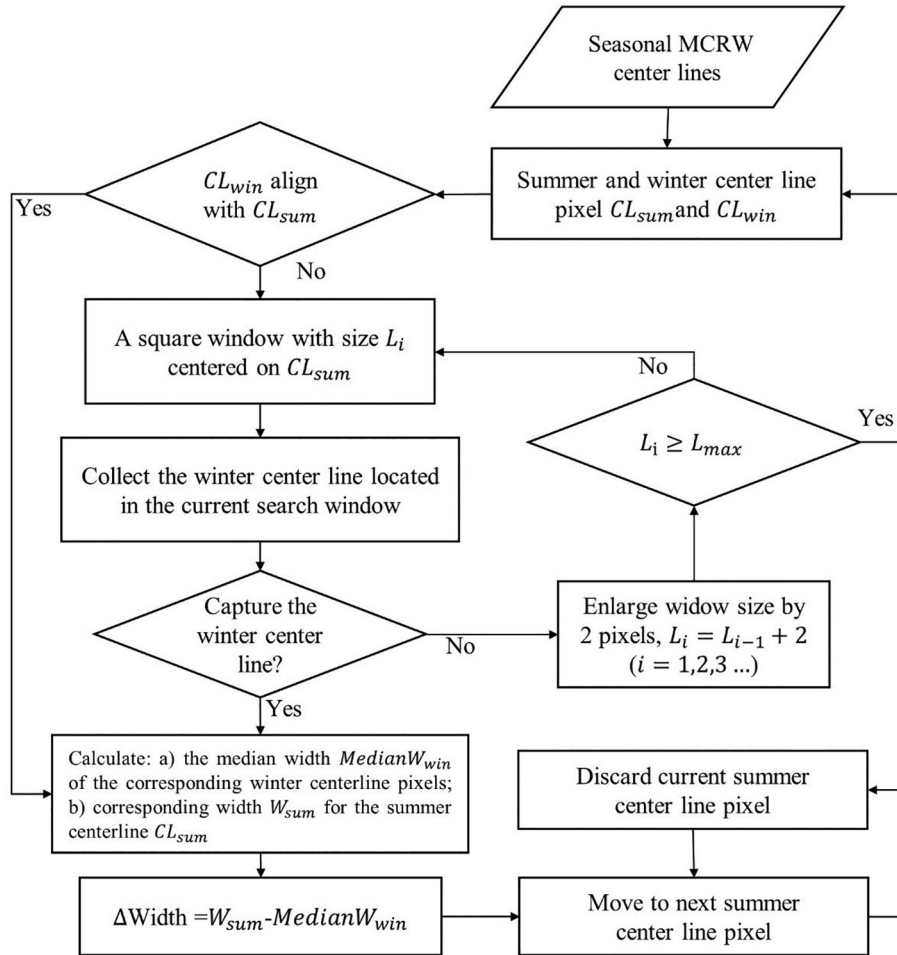
Fig. 5. Flowchart of the proposed locally adaptive search method to quantify river width variations when river center lines shift over time, taking the seasonal MCRW widths as an example.

automatically manage all the tiles for parallel execution and also to avoid the latency in the frequent instantiation and destruction of the processes. The number of processes maintained in the pool is tuned based on the computing resources available on a single machine, e.g., memory and processors. With 24 cores of dual Intel(R) Xeon(R) processors and 64 GB of memory, it took 12 days to process all 972 tiles in parallel with a pool of eight processes. Finally, we obtained the results retrieved from the individual tiles and aggregated them to generate the MCRW dataset.

3.2. Quantifying river width variations

MCRW provided multi-temporal information regarding both river width and channel center line. However, center lines shift over time due to streamflow variations or channel migration, making it difficult to quantify the variations of river width from planimetric river geomorphology data. We thus developed a locally adaptive search method to quantify river width variations when the center lines are misaligned. As shown in Fig. 5, the proposed approach first determines the location of the center line pixels of each period (e.g., summer and winter). If these center line pixels are aligned (i.e. the center line pixels in summer and winter share the same geographic location), the width variations can be defined using Eq. (2):

$$\Delta_{Width} = W_{T1} - W_{T2} \tag{2}$$

where W_{T1} and W_{T2} denote the river width in the different periods (i.e. summer and winter). Considering the fact that river center lines shift over time, we could not find aligned pixel pairs in a large number of

river channels. Thus, along the center lines in a given period, we attempted to collect the river widths measured at different periods (season or year) in a square window centered on the pixels of the base period (summer in this paper). The window size was enlarged by two pixels when the previous one failed to capture any center line pixel from other MCRW data. The iterative searching continued until the center line (measured at different periods) were found or the maximum window size was reached (11 pixels in this study). The river width variations were then determined as:

$$\Delta_{Width} = W_{T1} - Median\{W_{T2,1}, W_{T2,2},..., W_{T2,n}\} \tag{3}$$

where $Median$(A) represents the median of the set of river width A. W_{T1} means the river width of the base period, and $W_{T2,\,i}(i = 1,2,...,n)$ denotes a set of river widths collected by the proposed method from different periods. As the window size continues to increase, it is likely to bring in pixels from other rivers, while a larger window size may also result in a higher computational cost. Thus, 11 pixels (~330 m) was chosen as the stopping condition (i.e. the maximum window size), in view of the fact that more than 80% of the rivers measured less than 350 m wide (see Section 4.1 for details).

This window searching strategy ensured that width measurements that were spatially adjacent and shared similar hydrologic conditions were compared. Based on the aforementioned method, we further calculated the percent variation to depict the seasonal width variability:

$$(Width_{sum} - Width_{win})/(Width_{sum} + Width_{win}) \tag{4}$$

where $Width_{sum}$ and $Width_{win}$ denote the river width in summer and winter, respectively.
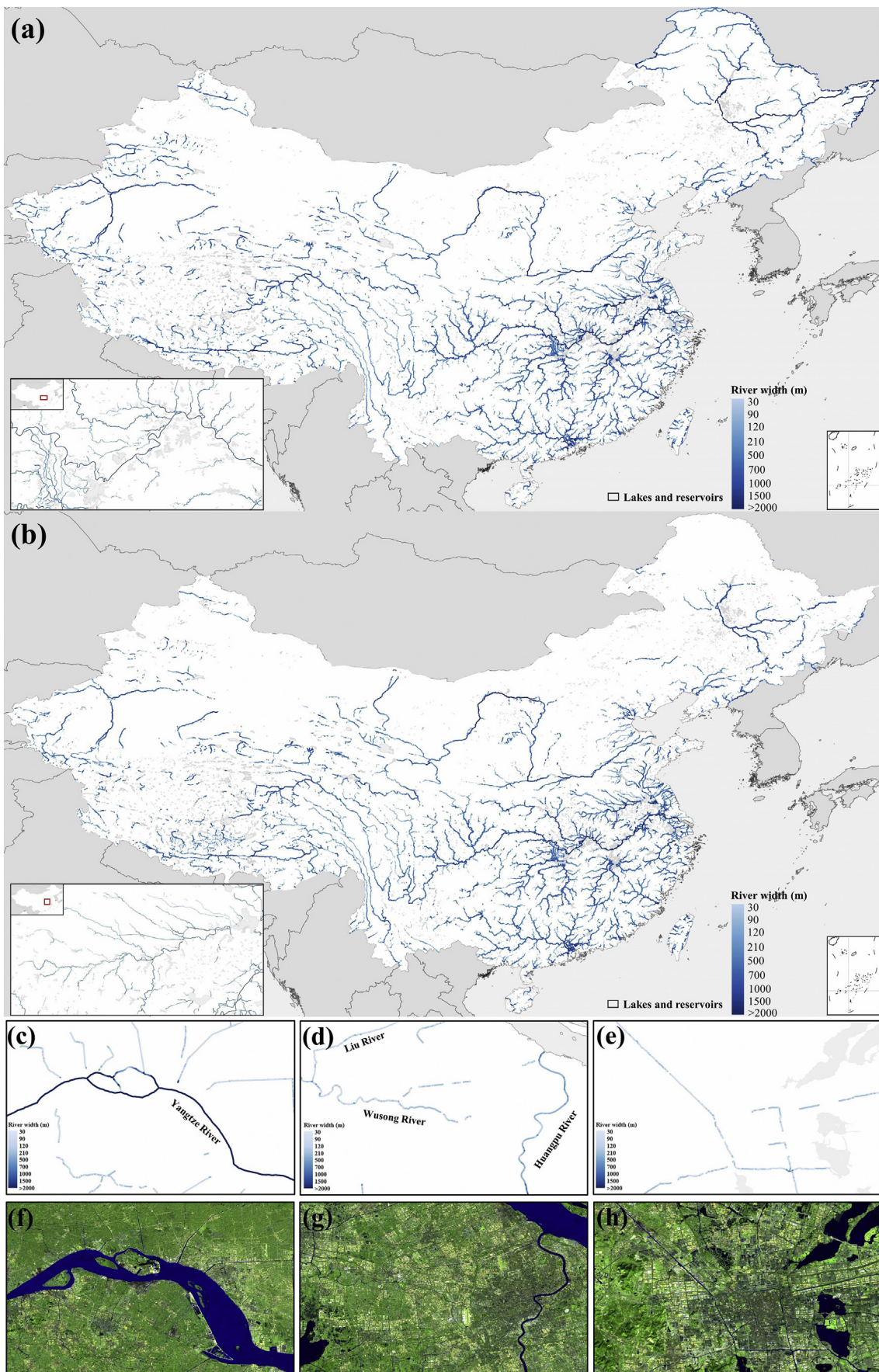
Fig. 6. The MCRW river width for: (a) summer 2005, with zoom-in map of Yangtze River (29.67 N, 112.99 E); (b) winter 2005, with zoom-in map of Huai River (32.83 N, 117.38 E). (c) Yangtze River (32.0345 N, 120.6221 E); (d) Wusong River and Huangpu River (31.2271 N, 121.3123 E); (e) canals in Suzhou City (31.3020 N, 120.6069 E); (f), (g) and (h) are the corresponding false colour composites of Landsat-8 images for (c), (d) and (e), respectively.
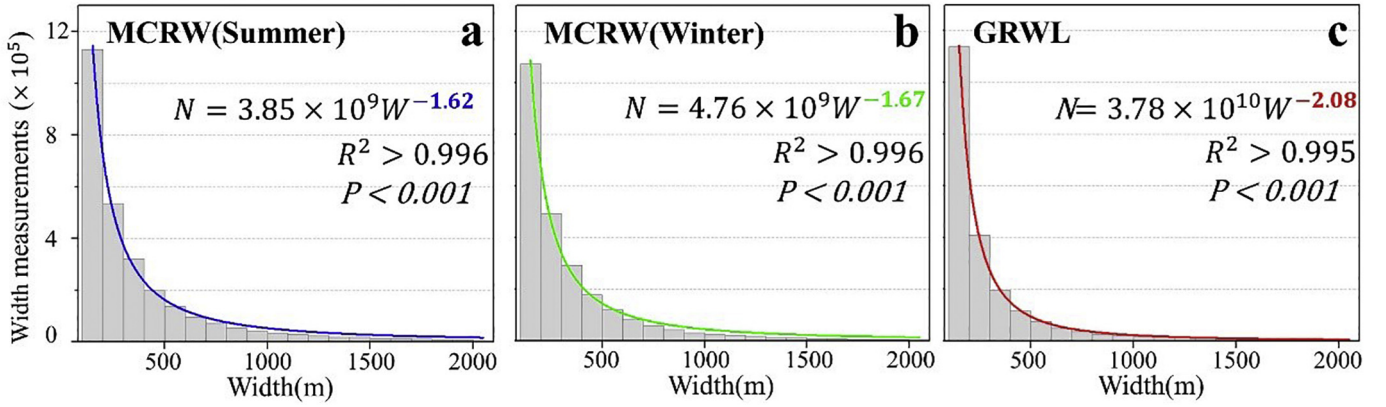
Fig. 7. River width distribution from 100 to 2000 m of summer/winter MCRW and GRWL.

4. Results and discussions

4.1. The multi-temporal China River width dataset

The MCRW dataset is made up of a total of 1.3×10^8 georeferenced planform measurements of river width in summer and winter (Fig. 6a and b) for the years of 1990, 1995, 2000, 2005, 2010, and 2015, representing 1.4×10^5 km of rivers in China. The MCRW river widths range from 30 m (i.e. the minimum pixel size of Landsat images) to 14,500 m (in the estuary where the Yangtze River meets the East China Sea; see Fig. 8a). Each measurement in the dataset consists of the latitude and longitude of the river center line pixel and its corresponding width. In summer, 3% of the rivers are wider than 2000 m, while more than 80% of the rivers are narrower than 350 m.

It was found that the distribution of the seasonal MCRW width (Fig. 7), which ranges from 100 m to 2000 m, closely ($R^2 > 0.99$, $p < 0.01$) follows the power-law function:

$$N_s = 3.85 \times 10^9 \, W_s^{-1.62} \tag{5}$$

$$N_w = 4.76 \times 10^9 \, W_w^{-1.67} \tag{6}$$

where N_s and N_w denote the number of pixels for corresponding river width W_s and W_w in summer and winter, respectively. Following Allen and Pavelsky (2015), we calculated the power-law function for GRWL river width (ranging from 100 m to 2000 m, $R^2 > 0.99$, $p < 0.01$):

$$N_{GRWL} = 3.78 \times 10^{10} \, W_{GRWL}^{-2.08} \tag{7}$$

where N_{GRWL} stands for the number of GRWL river width measurements (W_{GRWL}) in China. The fitted curves were generally similar, and our MCRW slightly outnumbered GRWL (Fig. 7). The GRWL-derived width distribution was characterized by a larger exponent (2.08 in Eq. (7)) than that of MCRW (1.62 and 1.67 for summer and winter estimates, respectively), indicating that the MCRW possessed a higher proportion of wider rivers (Allen and Pavelsky, 2015). The result can be explained as: i) MCRW retained center line for each channel while GRWL aggregated the multi-channel river into a single one; ii) different hydrological conditions of two datasets. Therefore, the number of the pixels of the river center lines was slightly different between MCRW and GRWL.

The MCRW dataset represents the first multi-temporal morphometric survey of Chinese rivers in summer/winter from 1990 to 2015, providing historical information regarding river center lines and widths in both raster and vector format. The raster files contain center line pixels with the value of the corresponding river width, while the vector files consist of polylines that connect each center line pixel to the adjacent ones.

4.2. Validation of the MCRW dataset

To assess the accuracy of the MCRW dataset, we compared the river widths with the corresponding in-situ records from the Hydrologic Yearbooks issued by the Ministry of Water Resources of China. A total of 59 reference gauging stations (Fig. 1) were chosen by considering the following criteria: (i) a station must have been operated for at least 10 years; (ii) the distance between the station to the nearest MCRW center line should be less than 1.5 km; and (iii) the station should have a complete seasonal record, without missing data in summer or winter. We aggregated all the in-situ records for the summer/winter season at each station and calculated the maximum, mean, and minimum seasonal widths. The corresponding seasonal in-situ width was then compared to the mean width of the five corresponding MCRW estimates that were the nearest to the current station, as conducted by Allen and Pavelsky (2015, 2018). In addition, we compared the produced MCRW estimates at 50% water occurrence with the GRWL estimates, considering that the latter was the only existing 30-m river width dataset for China and was composited using Landsat images captured at mean discharge.

We used the mean absolute percentage error (MAPE) to compare the MCRW estimates and GRWL estimates with the seasonal in-situ measurements:

$$MAPE = \frac{100\%}{n} \sum_{i=1}^{n} \left| \frac{W_i - \widehat{W_i}}{W_i} \right| \tag{8}$$

where W_i stands for the seasonal in-situ references, and $\widehat{W_i}$ denotes the MCRW or GRWL river width. In addition to the MAPE, the root-mean-square error (RMSE) and relative root-mean-square error (RRMSE) were also used to assess the accuracy:

$$RMSE = \sqrt[2]{\frac{1}{n} \sum_{i=1}^{n} (W_i - \widehat{W_i})^2} \tag{9}$$

$$RRMSE = \frac{RMSE}{\frac{1}{n} \sum_{i=1}^{n} W_i} \tag{10}$$

where W_i stands for the in-situ references, and $\widehat{W_i}$ denotes the MCRW- or GRWL-estimated river width.

From Table 3 and Fig. 9, it can be seen that, MCRW estimates showed the most satisfactory accuracy at 1% occurrence (i.e., the maximum width) in nearly all the situations. Therefore, it can be stated that MCRW can represent the temporal river width dynamic better (e.g., seasonal variability) and more practical for understanding the river dynamics.

Allen and Pavelsky, (2018) validated the GRWL with width measurements at gauging stations operated by United States Geological Survey (USGS) and Water Survey of Canada (WSC) in the North American. They achieved satisfactory RMSE (25.2 m) between GRWL

Table 3
Mean absolute percentage error (MAPE), root-mean-square error (RMSE) and relative root-mean-square error (RRMSE) for MCRW minimum (100% occurrence), mean (50% occurrence) and maximum (1% occurrence) estimates compared with minimum, mean and maximum in-situ width, respectively. GRWL estimates was compared with the mean width of in-situ data.

Metrics	Seasons	MCRW 1% occurrence	MCRW 50% occurrence	MCRW 100% occurrence	GRWL
MAPE	Summer	12.4%	14.0%	19.6%	17.9%
	Winter	17.7%	21.5%	34.0%	19.9%
	Total	15.0%	17.7%	26.2%	18.9%
RMSE (RRMSE)	Summer	67.6 m (13.5%)	59.8 m (13.0%)	116.2 m (27.8%)	121.5 m (26.4%)
	Winter	79.3 m (16.7%)	111.7 m (27.0%)	160.8 m (44.0%)	100.1 m (24.2%)
	Total	73.7 m (15.2%)	89.6 m (20.5%)	138.2 m (35.5%)	111.4 m (25.5%)

and North American in-situ widths. Please note that the in-situ measurements for North America (mean width of 109.2 m and median of 77.8 m) were different in scale to those of China (mean width of 440.7 m and median of 272 m). Therefore, RRMSE, which is a normalization of RMSE that is calculated via dividing the RMSE by the mean in-situ measurements, was introduced to facilitate the comparison between datasets validated with different in-situ measurements. In this manner, the RRMSE of MCRW at 50% occurrence (compared to the Chinese in-situ measurements) was 20.5%, which was better than the 23.1% of GRWL (compared to the North America in-situ measurements).

Although both MCRW and GRWL estimated the river width on the basis of the RivWidth method, GRWL surveyed the river widths that were close to mean discharge, since the widths were generated from cloudless Landsat tiles captured at mean discharge. MCRW, on the other hand, was produced by composited cloudless water maps under dynamic (i.e., minimum, mean, and maximum) water occurrence in summer/winter. Consequently, the differences in temporal coverage might account for the relatively poor performance of GRWL when compared to the seasonal in-situ measurements, especially given that seasonal precipitation varies greatly in China. As for the comparison between GRWL and the summer/winter in-situ measurements, RMSE and RRMSE were lower in winter (Table 3), indicating that the GRWL-estimated mean discharges at the locations of the in-situ measurements were more likely to be in winter (November to March in this study).

The total median bias of the MCRW estimates was 5 m, relative to in-situ width measurements. The errors possibly came from three sources: (i) the inaccuracies inherent in the GSW data; (ii) the errors of the RivWidth method; and (iii) the errors associated with the in-situ measurements. The primary source of uncertainty in MCRW is the GSW data. Although the validation with in-situ measurements suggests that MCRW represents accurate estimates of river width in summer/winter, there are clear instances where river widths are overrated due to misconnection with the surrounding paddy fields. In addition, width measurements of pixels at channel boundaries may be overestimated due to the difficulty in the classification of mixed pixels. The errors of RivWidth are mainly triggered by the predefined length of center line segment used to determine the flow direction. In highly sinuous rivers where flow directions change rapidly, the width measurements may be overestimated since the cross sections derived from the flow directions to each center line pixel are not completely orthogonal to the channel. Moreover, the positive values of MAPE and RRMSE also include other sources of error, such as the difference in acquisition time between the Landsat images and the in-situ measurements.

We aggregated the non-valid observations (e.g., cloud, snow, and missing data) to further assess the integrality of MCRW. Overall, the average proportion of non-valid observations was 2.39% and 22.47% in summer and winter, respectively. The relatively high non-valid

observation proportion in winter (Fig. 10a) can be attributed to the fact that: (i) snow and ice were categorized into non-valid observations in GSW; and (ii) the spatial coverage of the GSW data in northern and southern latitudes was limited during the winter. Please note that the proportion of non-valid observations in winter 1990 and 1995 was almost twice than that of 2000 (Fig. 10). The absence of valid observations is mainly due to the uneven spatial and temporal coverage of Landsat data. Prior to 2000, only Landsat 5 was operational, but it had no on-board data storage capabilities and its relay satellites failed in 1992 (Goward et al., 2006; Whitcraft et al., 2015), which limited the availability of Landsat data. This situation was improved after 1999 when Landsat 7 was commissioned and subsequently maintained a routine global acquisition plan (Arvidson et al., 2001; Goward and Cohen, 2004; Woodcock et al., 2008). Due to the lack of Landsat 5 data, the width measurements could be affected by the availability of valid observation to some extent. However, the proportion of non-valid observations for most drainage regions in summer is less than 10% throughout all the periods (Fig. 10b), while more than half of the regions show relatively high proportion of valid observations in winter (Fig. 10a). In addition, the non-valid observations are not synchronized to the river width variations (Fig. 11).

4.3. Spatiotemporal dynamics of river width

MCRW provided dynamic information regarding both river width and center lines. We designed a locally adaptive search method (see Section 3.2) to quantify river width variations when the center lines are misaligned. The method aimed to collect the river widths measured at different periods (season or year) in a square window. This window searching strategy ensures that width measurements that are spatially adjacent and share similar hydrologic conditions are compared. The same strategy can also be used to find the river widths measured at different periods for a given center line pixel. In this way, all the measurements for the same drainage region will be consistent throughout each study period, ensuring the comparability of the averaged river width. We used the MCRW estimates at the maximum water extent (i.e., 1% occurrence) to calculate the mean width of the nine major drainage regions to depict the spatiotemporal dynamics of river width in China from 1990 to 2015. The maximum width was adopted by considering that: i) it was more consistent to the measurements obtained by the gauging stations (Fig. 9); and ii) maximum water extent can reduce the data missing in early periods. From Fig. 11j, it can be seen that the mean river width of China in both summer and winter has increased over the past 25 years, with average growth rates of 1.603 m/year and 1.375 m/year for summer and winter, respectively. The mean river widths in summer for the YLR, YZR, PER, SLR, ILR, SWR, and SER regions have shown increasing trends ($0.34 \le R^2 \le 0.8$). In winter, the mean river widths for the YLR, YZR, PER, SLR, ILR, SWR, and SER basins have shown upward trends ($0.38 \le R^2 \le 0.76$), with significant ($p < .05$) upward trends in the YLR and ILR regions. Significant ($p < .05$) upward trends in the ILR regions were observed in both summer and winter, which can be linked to the increased run-off caused by accelerated glacier melt and higher annual precipitation in the Tibetan Plateau (Lutz et al., 2014).

Our results show that six major regions (i.e., YLR, YZR, PER, ILR, SWR, SER) exhibit increased river width from 1990 to 2015. The river width increase in these areas can be likely attributed to the increasing flood intensity (Zhang et al., 2015). The increased run-off caused by accelerated glacier melt and higher annual precipitation in the Tibetan Plateau (Lutz et al., 2014) may account for the increased river width in ILR, SWR and YZR. The increment of river width over PER, YZR, and ILR is probably linked to the more frequent PEPEs (persistent extreme precipitation events) after 1990 in midwestern and southern China (Chen et al., 2013). The increase of river width in ILR is also likely attributed to the significantly increased precipitation frequency and intensity in western China (Zhai et al., 2005). In contrast, the river
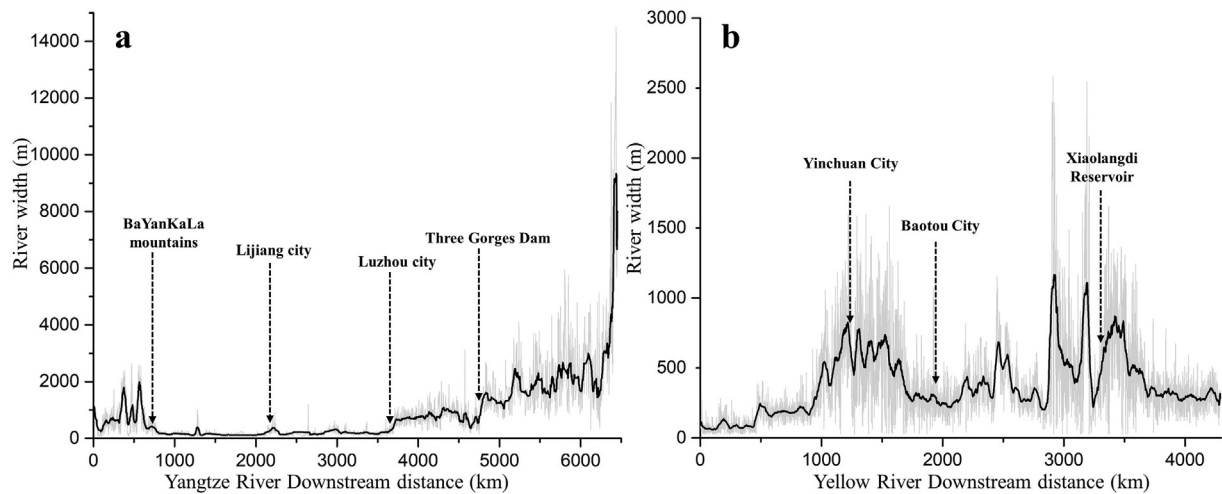
Fig. 8. Raw (gray) and smoothed (black) longitudinal widths along the mainstreams of Yangtze (a) and Yellow (b) River. (For interpretation of the references to colour in this figure legend, the reader is referred to the web version of this article.)

width declines in HAR and HHR, due to the decreased precipitation frequency/intensity (Zhai et al., 2005). Climate-related increment in river width can be also found in YZR, PER and SER, as these regions suffered from great floods around 1998 and their widths reached peaks around 2000 (Wang and Plate, 2002; Zong and Chen, 2000). In addition, the decline in runoff and river width over HAR is possibly also linked to the increasing demands for agricultural water consumption (Yang and Tian, 2009).

We performed least-squares regression over the multi-temporal MCRW data to depict the spatial distribution of the river width trend of summer (Fig. 12). As shown in Fig. 12a, while the river width for the upstream of the TGD increased from 1990 to 2015, the Yangtze River downstream of the TGD decreased in width. This is likely related to the drastically changed water and sediment processes after the impoundment of the TGD (Xu and Milliman, 2009; Yang et al., 2006). The operation of dams will alter the hydrologic regimes and thus change the hydrologic processes (Hu et al., 2008). Given a similar discharge condition, decrease of sediment can exacerbate the lateral erosion and subsequently increase the river width (Yang et al., 2015). Considering the notable reduction of sediment load in the lower YZR after the operation of the Three Gorges Dam (TGD) in 2003 (Xu and Milliman, 2009; Yang et al., 2006), our results show uptrends of river width in the upper/middle reaches of YZR while the width of its lower reaches decreased (Fig. 12a). This can be attributed to the construction and reinforcement of the levees and revetments along the Yangtze River after the great flood in 1998 (Yin and Li, 2001), which restricted lateral erosion in the channel. Obvious upward trends (~5 m/year) are observed in the Lancang River (Fig. 12b), Ya-lung River, Nu River, which can be linked to the growth of the number of cascade hydropower stations in these areas (Chang et al., 2010; Cheng et al., 2012). A host of hydropower stations are under-construction or planned along Lancang River, which might trigger some problems concerning the water resource management and ecosystem service in the lower reach of Lancang River (i.e., Mekong River). In general, our results demonstrate the impacts of climate change and climate perturbations on river width and the phenomenon that river width can be affected by human activities.

4.4. Seasonal variations of river width

Under the influence of the summer/winter Asian monsoons, channel widths in China show seasonal patterns. We also used the MCRW dataset at 1% occurrence (i.e., the maximum water extent) for 2015 to estimate the summer/winter river width variability. This indicated that the river widths of the middle YZR, lower YLR, lower PER, and upper/

middle SWR basins were wider in summer. Yangtze mainstream showed relatively small percent variability while its tributaries in Jianghan plain tended to vary more (zoom-in map of Fig. 13), which can be attributed to the fact that wider rivers (e.g., mainstream of Yangtze) tend to vary more in absolute variation but less in terms of percent variability.

While most rivers were wider in summer during the study period, larger width values were observed in winter in the middle reaches of the Yellow River and the upper reaches of the Black River (Fig. 13). The upper and middle reaches of the Yellow River locate in the northeastern edge of the Tibetan Plateau and Inner Mongolia (higher latitude), respectively. While the upstream part of the Yellow River thaws first in the early spring, the middle reaches are still frozen (Fig. S2). The upper stream carries ice into the still-frozen middle reaches, and ice jams are formed when broken chunks of ice pile up. Ice jams can cause inundation or even overbank flooding, which accounts for the wider channels measured from the satellite images in winter. A similar phenomenon was also found in another northerly flowing river in China, namely the Black River (Fig. 13). The seasonal width variations of the Yangtze River are mostly dominated by precipitation. Climatologically, sustained precipitation brought by the summer monsoon together with streamflow from the upper region cause a rise in the water level in the lower reaches of Yangtze River in early summer (Zong and Chen, 2000). Topographically, on the other hand, the relatively gentle stream gradient in the middle/lower YZR region slows down the flow velocity. The Yangtze mainstream in the lower basin is much wider than upstream of the TGD (Fig. 8a), and thus water is retained longer in the channels, which increases the possibility of capturing a wider river in summer from satellite observations.

4.5. Limitations and uncertainties

The spatial and temporal coverage of the MCRW dataset is limited by the input and the methods. Although we fixed the seasonal windows according to the East Asia summer/winter monsoons, this approach could easily be transferred to other basins or regions, based on the local precipitation variations. For example, the approximate rainy/dry season for each basin could be estimated via long-term discharge data, such as the data available from the Global Runoff Data Centre.

In this study, we extended the seasonal windows due to the missing data inherent to GSW data in winter. Generally speaking, more valid observations were available during the winter season (Asner, 2001). However, GSW data were not always available for the winter. For example, the GSW data covered 78 N to 40 S in July but 32 N to 56 S in
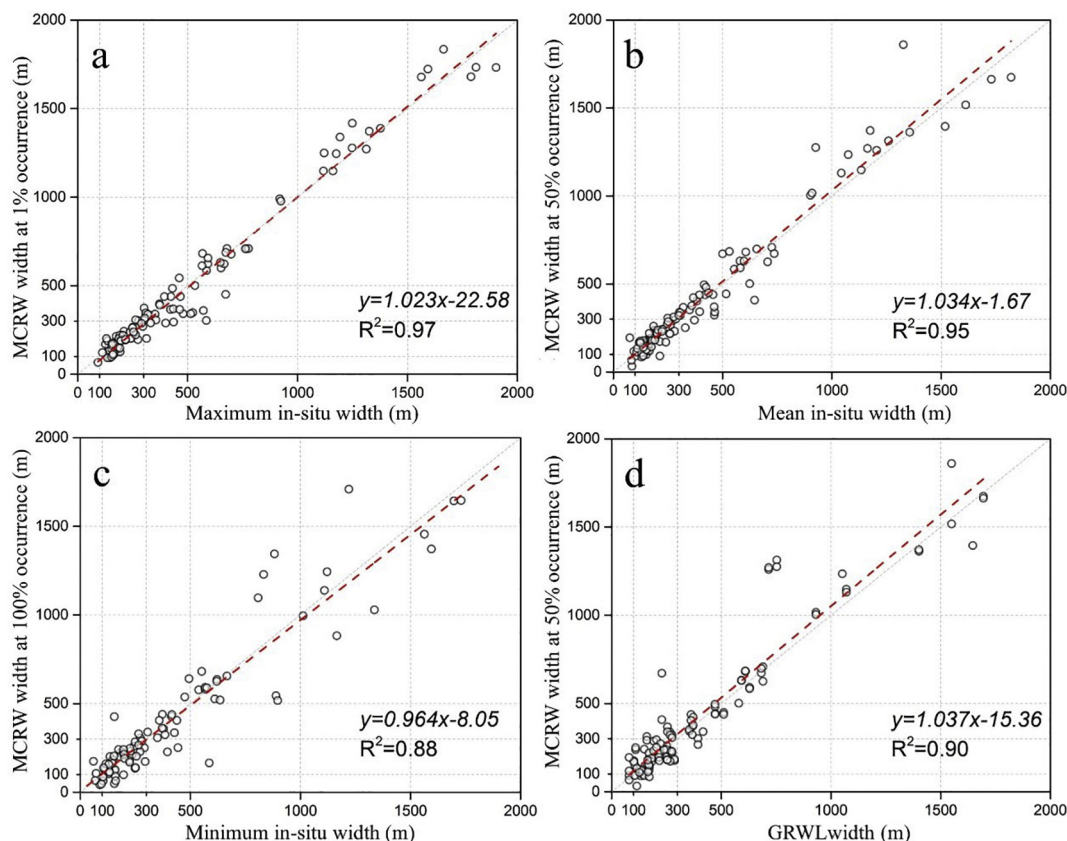
Fig. 9. Comparisons: (a) MCRW maximum width (1% occurrence) against the maximum in-situ width (Pearson's correlation: 0.98, $p < .05$); (b) MCRW mean width (50% occurrence) against the mean in-situ width (Pearson's correlation: 0.98, $p < .05$); (c) MCRW minimum width (100% occurrence) against the minimum in-situ width (Pearson's correlation: 0.93, $p < .05$); (d) GRWL width at mean discharge against the MCRW mean width (50% occurrence) (Pearson's correlation: 0.95, $p < .05$).

January. The pattern of missing data was also different in different months. According to Pekel et al., (2016), water detection was only conducted on scenes where the solar elevation was above 30 degrees to avoid the effects of low illumination. Thus, missing data were found in both northern and southern latitudes during the winter. Moreover, Landsat 7 and Landsat 8 maintained routine global acquisition plans (Long Term Acquisition Plans, LTAPs), aiming at capturing the significant changes of the Earth's surface (Arvidson et al., 2006). In LTAPs,

high-latitude images were not scheduled for acquisition during the winter season when the sun angle was lower than a certain threshold, which limits the availability of Landsat data in winter (Arvidson et al., 2001).

In addition, in this study, while the use of reservoir and lake database eliminated most water bodies connected to rivers, some water bodies (e.g., impoundments and irrigation areas) may be included in the width estimation. However, they are considered conceptually part
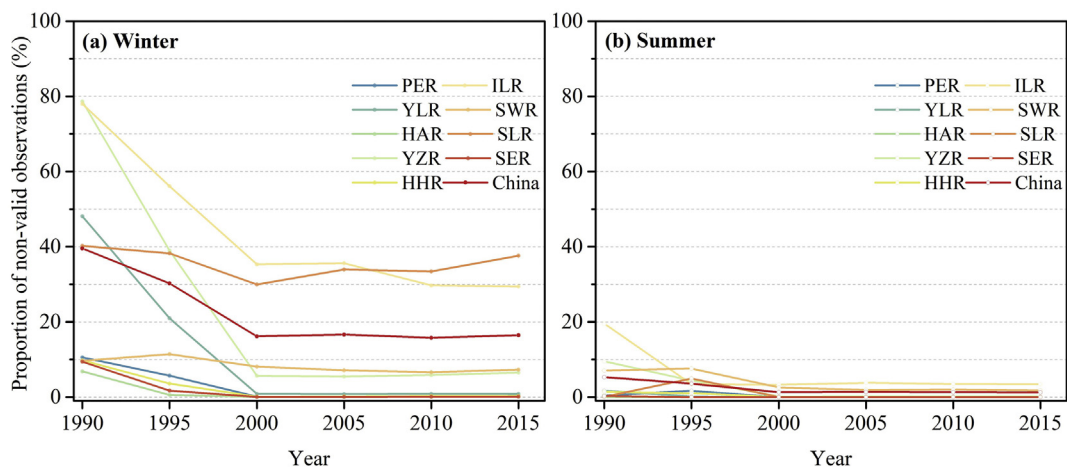

Fig. 10. Proportion (%) of non-valid observations in winter (a) and summer (b) for the Yellow River region (YLR), the Yangtze River region (YZR), the Pearl River region (PER), the Songliao River region (SLR), the Hai River region (HAR), the Inland River region (ILR), the Huai River region (HHR), the South-West River region (SWR), the South-East River region (SER) and China. (For interpretation of the references to colour in this figure legend, the reader is referred to the web version of this article.)
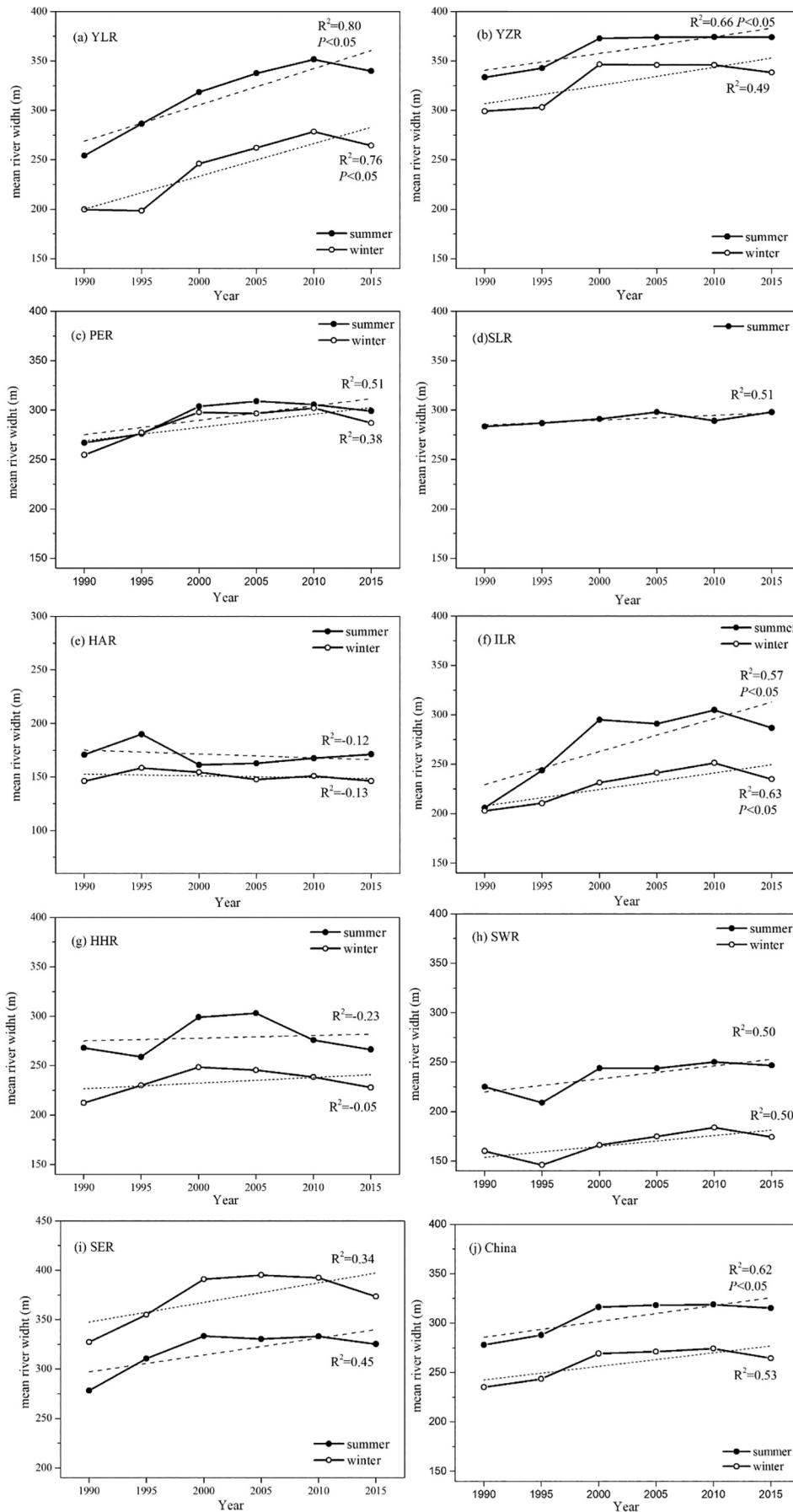
Fig. 11. Temporal dynamics of river width derived from the MCRW dataset for: (a) the Yellow River region (YLR); (b) the Yangtze River region (YZR); (c) the Pearl River region (PER); (d) the Songliao River region (SLR); (e) the Hai River region (HAR); (f) the Inland River region (ILR); (g) the Huai River region (HHR); (h) the South-West River region (SWR); (i) the South-East River region (SER); and (j) China from 1990 to 2015. The mean river width of the SLR region in winter was excluded due to the lack of valid observations. (For interpretation of the references to colour in this figure legend, the reader is referred to the web version of this article.)
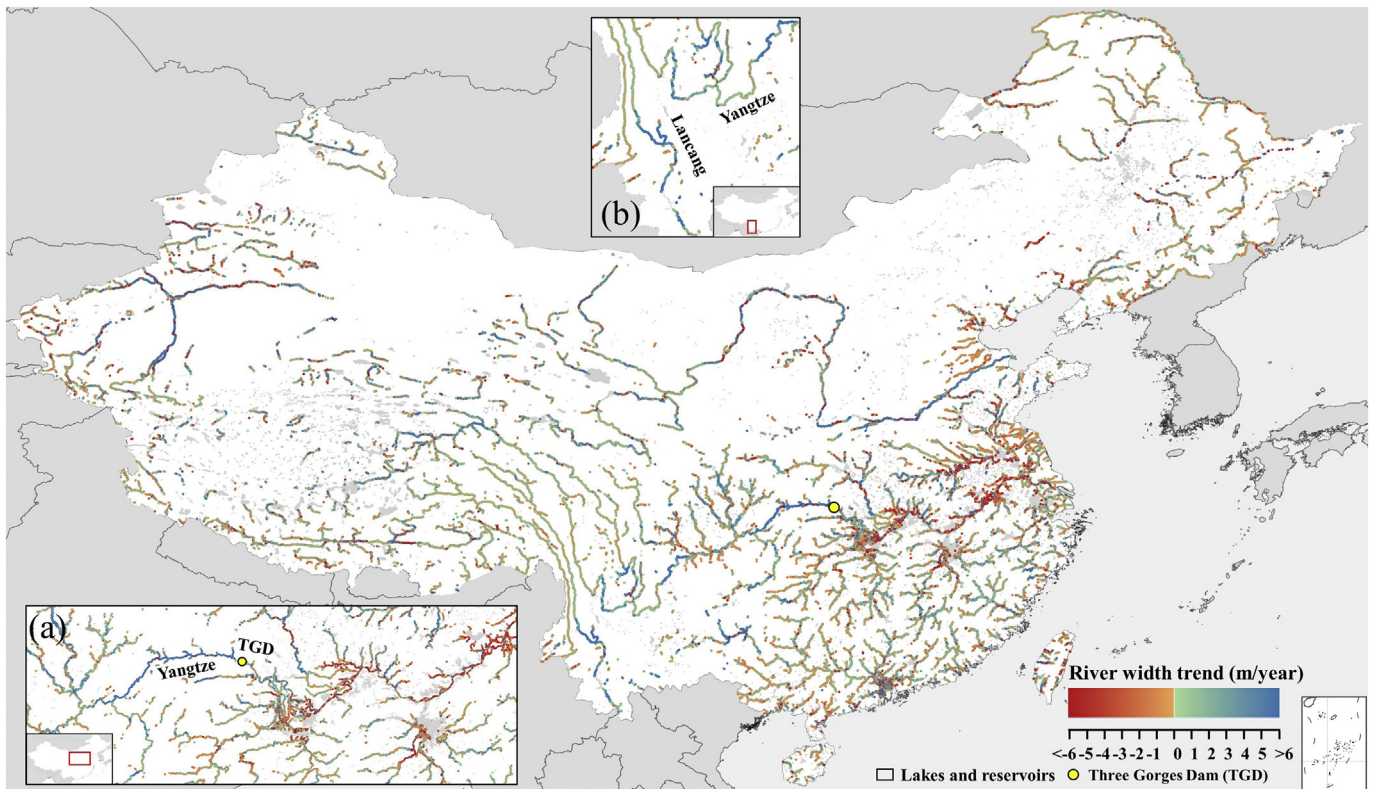
Fig. 12. The spatial distribution of the summer river width trend from 1990 to 2015 derived from the MCRW dataset, with zoom-in maps of (a) middle/lower reaches of Yangtze River (112.17 E, 29.69 N) and (b) middle reaches of Lancang River (110.70 E, 25.21 N).
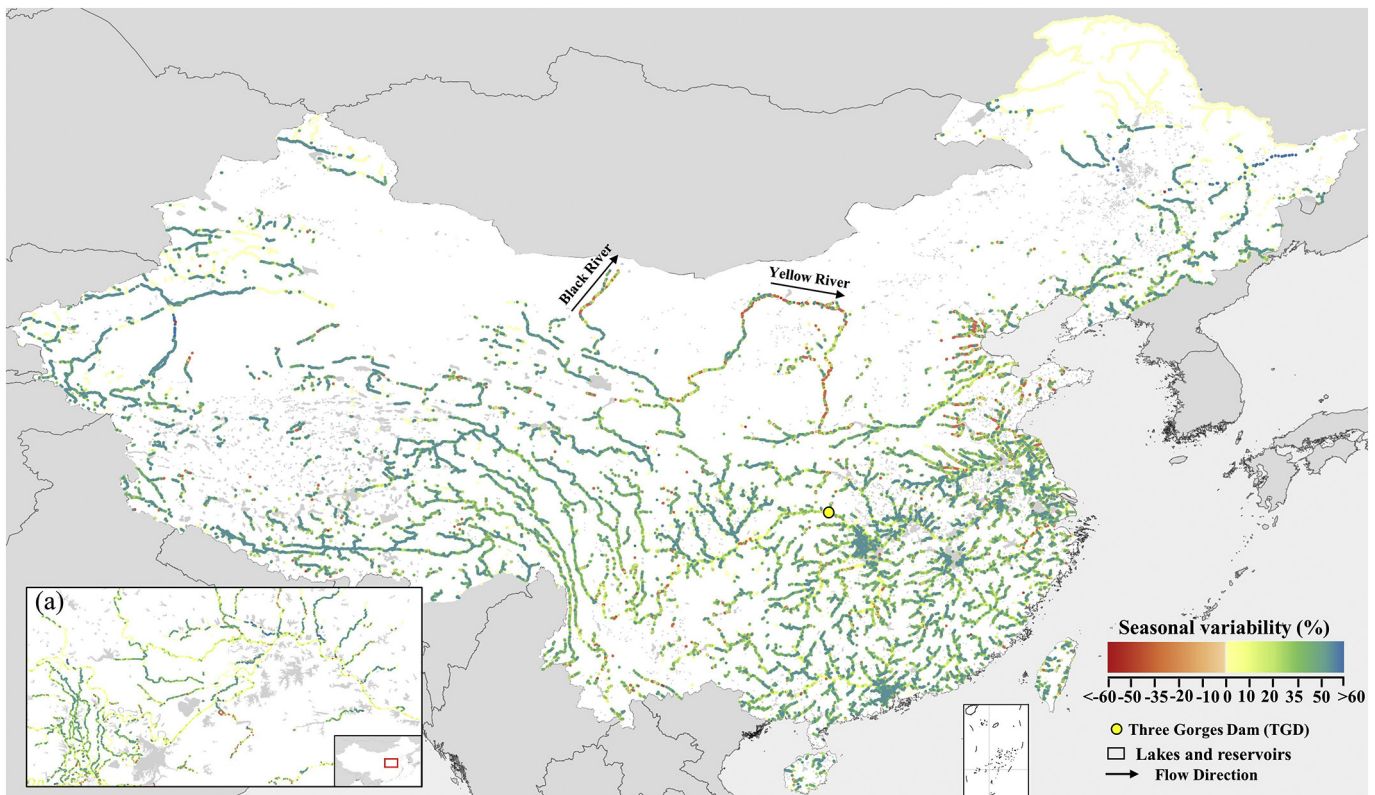

Fig. 13. Spatial distribution of seasonal river width variability, with zoom-in maps of (a) middle/lower reaches of Yangtze River (29.94 N, 113,75 E). The positive value suggests that river is wider in summer, while a negative value indicates a larger width value in winter.

of the river during inundation (Hou et al., 2019), since they are physically connected to the river channels. Besides, the islands and sandy bars were filled so as to avoid the possible overestimation in braided rivers, which, however, may affect the delineation of center line of these rivers. This source of uncertainties may be suppressed in the future by representing a center line using cubic splines as suggested by Miller et al. (2014).

The temporal coverage of the MCRW dataset is currently limited from 1990 to 2015, due to the availability of the GSW data. Pekel et al. (2016) have provided the parameters and details of the expert system that was used to generate the GSW data. Therefore, we can conveniently employ the classifier they provided to update the GSW water maps in future.

In addition, subject to the discernable resolution (30 m) of Landsat imagery, the width of some narrow channels can be undetected or partly detected, e.g., in the headwaters of the Yangtze or the Yellow Rivers. In future work, we can employ higher resolution images (e.g., 10-m resolution Sentinel images from European Space Agency) to further address this issue. The objective of this research, however, is to generate a multi-temporal dataset of China. To this aim, Landsat images are appropriate data sources due to their fine spatial resolution and long-term temporal span.

5. Conclusion

River width is a fundamental parameter for hydrological and hydraulic modeling. While the derivation of river width from satellite images is increasingly recognized (e.g., Allen and Pavelsky, 2018), multi-temporal river widths and their spatiotemporal dynamics obtained by the remote sensing approach have rarely been investigated in the current literature. In this paper, we have presented the Multi-temporal China River Width (MCRW) dataset, which makes the following contributions:

1) While the currently available products mainly focus on the river width on mean discharge (e.g., Allen and Pavelsky, 2015; Allen and Pavelsky, 2018), the MCRW dataset is the first to incorporate multi-temporal river width in China from 1990 to 2015 at a 5-year interval. In addition, we pay special attention to the seasonal variation, given that seasonal precipitation in China is dominated by the East Asian summer/winter monsoons.
2) A locally adaptive searching method was proposed to quantify river width variations when center lines were misaligned, based on which we further analyzed the spatial-temporal patterns and seasonal variations of river width of China. Our results show the impacts of climate fluctuations and climate perturbations on river width and the phenomenon that river width can be affected by human activities.
3) We improved the RivWidth algorithm by implementing a series of optimized strategies, such as (i) saving memory and computational time; and (ii) preserving the channel structures.

The MCRW dataset was validated by a comparison with in-situ measurements and the existing datasets. The analysis of the MCRW dataset indicated that the mean river width in China for both summer and winter has increased over the past 25 years. The river widths of the mainstream of the Yangtze River in the lower drainage region have shown a downward trend, while the middle reaches and tributaries (upstream of the TGD) have shown an upward trend. Further analysis of the seasonal variability found that rivers were generally wider in summer than in winter and Yangtze tributaries trended to vary more than its mainstream in middle/lower reaches. Temporal river width dynamic is very important for understanding river dynamics. As there are increasing hydrological or hydraulic modeling studies using vectorized river network (Lin et al., 2019), our findings and dynamic river width data would provide important reference for the modeling studies.

This paper has provided the first multi-temporal river width dataset with particular focuses on seasonal fluctuations and dynamic water occurrence, and to the best of our knowledge, it is the first study to reveal the spatiotemporal dynamics and seasonal variations of river widths in China by the use of satellite images. This product, combined with other data (e.g., precipitation, runoff, and sediment load data), will allow for more comprehensive characterization of channel form variations.

Declaration of Competing Interest

The authors declare that they have no known competing financial interests or personal relationships that could have appeared to influence the work reported in this paper.

Appendix A. Supplementary data

Supplementary data to this article can be found online at https://doi.org/10.1016/j.rse.2020.111918.

References

Allen, G.H., Pavelsky, T.M., 2015. Patterns of river width and surface area revealed by the satellite-derived North American River Width data set. Geophys. Res. Lett. 42, 395–402.
Allen, G.H., Pavelsky, T.M., 2018. Global extent of rivers and streams. Science. 361, 585.
Alsdorf, D., et al., 2003. The need for global, satellite-based observations of terrestrial surface waters. Eos, Trans. Am. Geophys. Union. 84, 269–276.
Alsdorf, D.E., et al., 2007. Measuring surface water from space. Rev. Geophys. 45.
An, Z., et al., 1990. The long-term paleomonsoon variation recorded by the loess-paleosol sequence in Central China. Quatern. Int. 7 (8), 91–95.
Andreadis, K.M., et al., 2013. A simple global river bankfull width and depth database. Water Resour. Res. 49, 7164–7168.
Arvidson, T., et al., 2001. Landsat 7's long-term acquisition plan — an innovative approach to building a global imagery archive. Remote Sens. Environ. 78, 13–26.
Arvidson, T., et al., 2006. Landsat-7 long-term acquisition plan. Photogramm. Eng. Remote Sens. 72, 1137–1146.
Asner, G.P., 2001. Cloud cover in Landsat observations of the Brazilian Amazon. Int. J. Remote Sens. 22, 3855–3862.
Azzari, G., Lobell, D.B., 2017. Landsat-based classification in the cloud: an opportunity for a paradigm shift in land cover monitoring. Remote Sens. Environ. 202, 64–74.
Barefoot, E., et al., 2019. Temporally variable stream width and surface area distributions in a headwater catchment. Water Resour. Res. 55, 7166–7181.
Bastviken, D., et al., 2011. Freshwater methane emissions offset the continental carbon sink. Science. 331, 50.
Battin, T.J., et al., 2008. Biophysical controls on organic carbon fluxes in fluvial networks. Nat. Geosci. 1, 95.
Biancamaria, S., et al., 2009. Large-scale coupled hydrologic and hydraulic modelling of the Ob river in Siberia. J. Hydrol. 379, 136–150.
Burn, D.H., 1999. Perceptions of flood risk: a case study of the Red River Flood of 1997. Water Resour. Res. 35, 3451–3458.
Chang, X., et al., 2010. Hydropower in China at present and its further development. Energy 35, 4400–4406.
Cheng, C.-T., et al., 2012. Operation challenges for fast-growing China's hydropower systems and respondence to energy saving and emission reduction. Renew. Sust. Energ. Rev. 16, 2386–2393.
Chen, Y., Zhai, P., et al., 2013. Persistent extreme precipitation events in China during 1951-2010. Clim. Res. 57, 143–155.
Donchyts, G., et al., 2016. Earth's surface water change over the past 30 years. Nat. Clim.

Chang. 6, 810.

Gleason, C.J., Smith, L.C., 2014. Toward global mapping of river discharge using satellite images and at-many-stations hydraulic geometry. Proc. Natl. Acad. Sci. 111, 4788.

Gorelick, N., et al., 2017. Google earth engine: planetary-scale geospatial analysis for everyone. Remote Sens. Environ. 202, 18–27.

Goward, S.N., Cohen, W.B., 2004. Landsat's role in ecological applications of remote sensing. BioScience. 54, 535–545.

Goward, S., et al., 2006. Historical record of Landsat global coverage. Photogramm. Eng. Remote Sens. 72, 1155–1169.

Grinand, C., et al., 2013. Estimating deforestation in tropical humid and dry forests in Madagascar from 2000 to 2010 using multi-date Landsat satellite images and the random forests classifier. Remote Sens. Environ. 139, 68–80.

Gurnell, A.M., 1997. Channel change on the River Dee meanders, 1946–1992, from the analysis of air photographs. Regulated Rivers 13, 13–26.

Hannah, D.M., et al., 2011. Large-scale river flow archives: importance, current status and future needs. Hydrol. Process. 25, 1191–1200.

Hou, J., et al., 2018. Using modelled discharge to develop satellite-based river gauging: a case study for the Amazon Basin. Hydrol. Earth Syst. Sci. 22, 6435–6448.

Hou, J., et al., 2019. Hydromorphological attributes for all Australian river reaches derived from Landsat dynamic inundation remote sensing. Earth Syst. Sci. Data. 11, 1003–1015.

Hou, J., et al., 2020. Global satellite-based river gauging and the influence of river morphology on its application. Remote Sens. Environ. 239, 111629.

Hrachowitz, M., et al., 2013. A decade of Predictions in Ungauged Basins (PUB)-a review. Hydrolog. Sci. J. 58, 1198–1255.

Hu, W.-w., et al., 2008. The influence of dams on ecohydrological conditions in the Huaihe River basin, China. Ecol. Eng. 33, 233–241.

Isikdogan, F., et al., 2017. RivaMap: an automated river analysis and mapping engine. Remote Sens. Environ. 202, 88–97.

Lehner, B., Döll, P., 2004. Development and validation of a global database of lakes, reservoirs and wetlands. J. Hydrol. 296, 1–22.

Lehner, B., et al., 2008. New global hydrography derived from spaceborne elevation data. Eos, Trans. Am. Geophys. Union 89, 93–94.

Lehner, B., et al., 2011. High-resolution mapping of the world's reservoirs and dams for sustainable river-flow management. Front. Ecol. Environ. 9, 494–502.

Lin, P., et al., 2019. Global reconstruction of naturalized river flows at 2.94 million reaches. Water Resour. Res. 55, 6499–6516.

Lin, P., et al., 2020. Global estimates of reach-level Bankfull River width leveraging big data geospatial analysis. Geophys. Res. Lett. 47 (7) e2019GL086405.

Lück, W., van Niekerk, A., 2016. Evaluation of a rule-based compositing technique for Landsat-5 TM and Landsat-7 ETM+ images. Int. J. Appl. Earth Obs. Geoinf. 47, 1–14.

Lutz, A.F., et al., 2014. Consistent increase in High Asia's runoff due to increasing glacier melt and precipitation. Nat. Clim. Chang. 4, 587–592.

Marr, D., et al., 1980. Theory of edge detection. In: Proceedings of the Royal Society of London. Series B. Biological Sciences. 207. pp. 187–217.

Miller, Z.F., et al., 2014. Quantifying river form variations in the Mississippi Basin using remotely sensed imagery. Hydrol. Earth Syst. Sci. 18, 4883–4895.

Monegaglia, F., et al., 2018. Automated extraction of meandering river morphodynamics from multitemporal remotely sensed data. Environ. Model Softw. 105, 171–186.

Mueller, N., et al., 2016. Water observations from space: mapping surface water from 25years of Landsat imagery across Australia. Remote Sens. Environ. 174, 341–352.

de Paiva, R.C.D., et al., 2013. Large-scale hydrologic and hydrodynamic modeling of the Amazon River basin. Water Resour. Res. 49, 1226–1243.

Pavelsky, T.M., Smith, L.C., 2008. RivWidth: a software tool for the calculation of river widths from remotely sensed imagery. IEEE Geosci. Remote Sens. Lett. 5, 70–73.

Pekel, J.-F., et al., 2016. High-resolution mapping of global surface water and its long-term changes. Nature. 540, 418.

Raymond, P.A., et al., 2013. Global carbon dioxide emissions from inland waters. Nature.

503, 355.

Rosenfeld, A., Pfaltz, J.L., 1968. Distance functions on digital pictures. Pattern Recogn. 1, 33–61.

Sichangi, A.W., et al., 2016. Estimating continental river basin discharges using multiple remote sensing data sets. Remote Sens. Environ. 179, 36–53.

Sun, W., et al., 2018. Calibrating a hydrological model in a regional river of the Qinghai–Tibet plateau using river water width determined from high spatial resolution satellite images. Remote Sens. Environ. 214, 100–114.

Tang, Q., 2020. Global change hydrology: terrestrial water cycle and global change. Science China Earth Sciences. 63, 459–462.

Tang, Q., et al., 2009. Remote sensing: hydrology. Prog. Phys. Geogr. 33, 490–509.

Tarpanelli, A., et al., 2019. Daily River discharge estimates by merging satellite optical sensors and radar altimetry through artificial neural network. IEEE Trans. Geosci. Remote Sens. 57, 329–341.

The Ad Hoc Group, et al., 2001. Global water data: A newly endangered species. Eos, Trans. Am. Geophys. Union 82, 54–58.

Van Dijk, A.I.J.M., Renzullo, L.J., 2011. Water resource monitoring systems and the role of satellite observations. Hydrol. Earth Syst. Sci. 15, 39–55.

Van Dijk, A.I.J.M., et al., 2016. River gauging at global scale using optical and passive microwave remote sensing. Water Resour. Res. 52, 6404–6418.

Wang, B., Ho, Lin, 2002. Rainy Season of the Asian–Pacific Summer Monsoon. J. Climate 15, 386–398.

Wang, Z.-Y., Plate, E.J., 2002. Recent flood disasters in China. Proc. Inst. Civil Eng. 154, 177–188.

Whitcraft, A.K., et al., 2015. Cloud cover throughout the agricultural growing season: impacts on passive optical earth observations. Remote Sens. Environ. 156, 438–447.

Wilson, M., et al., 2007. Modeling large-scale inundation of Amazonian seasonally flooded wetlands. Geophys. Res. Lett. 34.

Woodcock, C.E., et al., 2008. Free access to Landsat imagery. Science 320, 1011.

Wulder, M.A., et al., 2016. The global Landsat archive: status, consolidation, and direction. Remote Sens. Environ. 185, 271–283.

Xu, H., 2006. Modification of normalised difference water index (NDWI) to enhance open water features in remotely sensed imagery. Int. J. Remote Sens. 27, 3025–3033.

Xu, K., Milliman, J.D., 2009. Seasonal variations of sediment discharge from the Yangtze River before and after impoundment of the Three Gorges Dam. Geomorphology. 104, 276–283.

Xu, K., et al., 2004. Estimating river discharge from very high-resolution satellite data: a case study in the Yangtze River, China. Hydrol. Process. 18, 1927–1939.

Yamazaki, D., et al., 2012. Analysis of the water level dynamics simulated by a global river model: a case study in the Amazon River. Water Resour. Res. 48.

Yamazaki, D., et al., 2014. Development of the global width database for large Rivers. Water Resour. Res. 50, 3467–3480.

Yang, Y., Tian, F., 2009. Abrupt change of runoff and its major driving factors in Haihe River Catchment, China. J. Hydrol. 374, 373–383.

Yang, Z., et al., 2006. Dam impacts on the Changjiang (Yangtze) Tiver sediment discharge to the sea: the past 55 years and after the Three Gorges Dam. Water Resour. Res. 42.

Yang, C., et al., 2015. Remotely sensed trajectory analysis of channel migration in lower Jingjiang reach during the period of 1983–2013. Remote Sens. 7, 16241–16256.

Yang, X., et al., 2019. RivWidthCloud: an automated Google earth engine algorithm for river width extraction from remotely sensed imagery. IEEE Geosci. Remote Sens. Lett. 1–5.

Yin, H., Li, C., 2001. Human impact on floods and flood disasters on the Yangtze River. Geomorphology. 41, 105–109.

Zhai, P., et al., 2005. Trends in Total precipitation and frequency of daily precipitation extremes over China. J. Clim. 18, 1096–1108.

Zhang, Q., et al., 2015. Spatiotemporal behavior of floods and droughts and their impacts on agriculture in China. Global Planet. Change 131, 63–72.

Zong, Y., Chen, X., 2000. The 1998 Flood on the Yangtze, China. Nat. Haz. 22, 165–184.